Original Research Article

Magnetic Characterization of Co and Zn Nano Ferrites: Property Consideration for Oil-Spill Clean up

ABSTRACT

Nano-magnetic particles are significantly finding applications in environmental remediation. This work studied the magnetic properties of Co and Zn nano-ferrites, $CoFe_2O_4$ and $ZnFe_2O_4$ respectively, with considerations for the properties that are desirable for oil spill cleanup. The ferrite nanoparticles were synthesized by the glycol-thermal method at 200 ºC for 6 hours using a stirred pressure reactor. Single phase spinel crystal structures were obtained for both samples as determined by an X-ray diffraction (XRD) machine. The high-resolution transmission electron microscope and surface electron microscope images showed nano structures. The magnetic properties and magnetic hyperfine parameters were determined using a lakeshore vibrating sample magnetometer and ^{57}Fe Mössbauer spectroscopy. The XRD peaks were consistent with that of a single phase spinel structure. No impurity phase was detected. The nano-ferrites have crystallite sizes of about 10 nm and 17 nm for $CoFe_2O_4$ and $ZnFe_2O_4$. The nano almost-spherical nature of the samples was also confirmed from their morphology studies. The saturation magnetization of $CoFe_2O_4$ and $ZnFe_2O_4$ were about 50 emu/g and 30 emu/g respectively. They both exhibited superparamagnetic properties with a component of para-magnetism observed in $ZnFe_2O_4$ nano-ferrites. $CoFe_2O_4$ nano-ferrites exhibited better desired property for oil spill cleanup. The $ZnFe_2O_4$ nano-ferrites showed tendencies of slow response to magnetic field, however, it is more environmentally friendly. The magnetic hyperfine parameters and the isomer shift values for $CoFe_2O_4$ and $ZnFe_2O_4$ showed strong internal magnetic fields and the obtained values are consistent with spinel structure. The oxidation state of Fe was observed to be Fe^{3+}. Due to the low coercivity and high magnetization values, these particles could be considered as potential candidates for oil spill cleanup. These desirable magnetic properties will improve the recyclability of the nanoparticles using low applied magnetic fields.

Keywords: Glycol-Thermal, Single Phase Spinel, Superparamagnetic, Coercivity, ^{57}Fe Mössbauer Spectroscopy

1.0 INTRODUCTION

The emergence of nanotechnology has revolutionized innovations in almost all fields of endeavors such as in agriculture, pharmaceuticals, medicals, electronics, energy, environmental management, the oil and gas industry, aerospace and automobile [1]. It is an interdisciplinary technology that involves the application of materials with a size range of

about 1-100 nm, known as nanomaterials [2]. The unique properties derived from nanomaterials found interesting applications compared to their bulk counterpart. This is primarily due to the nano-size effect which gives nanomaterials a high surface to volume ratio, increased number of surface atoms and enhanced reactivity [3]. Magnetic, optical, and electrical properties at the nano-scale behave very differently from the bulk samples. The understanding of these properties has enabled the deployment of nanotechnology in the oil and gas industries in areas such as exploration, drilling, logging, hydraulic fracturing, formation damage, enhanced oil recovery (EOR) and ex-situ upgrading of oil shales/bitumen [2-5]. A more recent possible application of nanomaterials for environmental remediation is found in the oil and gas sector, which involves the use of amine functionalized or polymer coated magnetic nanoparticles for cleaning crude oil spills [3]. Therefore, there are enormous potentials in understanding the behavior of materials at nano-scale so that the properties can be tailored towards specific application.

The cubic spinel ferrites are one of such materials that are suitable for environmental remediation application. Ferrites belong to a special class of ceramic oxides which generally has a chemical formula of AB_2O_4. *A* represents one or more of the divalent transition metals, for example zinc (Zn), iron (Fe), magnesium (Mg), nickel (Ni), cobalt (Co), copper (Cu), or calcium (Ca) [6], and *B* represents solely iron (Fe). Generally, a cubic spinel structure consists of two interstitial sites known as tetrahedral *A* and octahedral *B* ions which contains 8 tetrahedral coordinated sites and 16 octahedral coordinated sites for divalent & trivalent metal cation occupancy, where *A* and *B* denote divalent and trivalent cations respectively [7-8]. For an ideal normal spinel of $ZnFe_2O_4$ ferrites, Zn^{2+} exclusively occupies the tetrahedral *A*-sites while Fe^{3+} occupies the octahedral *B*-sites. A mixed cation distribution is the case for $MgFe_2O_4$. Such distributions of cations significantly influence the magnetic properties of the ferrites [9].

A generic example is $C_xD_{1-x}Fe_2O_4$ where, $0 \leq x \leq 1$. At both extreme conditions for x = 0 or x = 1, DFe_2O_4 or CFe_2O_4 ferrites are obtained respectively. However, an intermediate case is obtained for x = 0.5 as is the case for $C_{0.5}D_{0.5}Fe_2O_4$ ferrite. Consequently, one could vary the structural and magnetic properties of the ferrite by establishing different intermediate cases. Also, the method of synthesis could also have effect on the magnetic properties of nanoparticles [10].

The current project synthesized single phase nanoparticles of $CoFe_2O_4$ and $ZnFe_2O_4$ ferrites using the glycol-thermal synthesis method. The selected elements such as Fe and Zn are environmentally friendly. However, Zn has low anisotropy compared to Co.

Therefore, Co is selected because of its high anisotropy so as to improve the magnetization of the sample and help in making comparison.

2. THEORETICAL BACKGRAOUND

High saturation magnetization M_S and low coercivity H_C are characteristic features of superparamagnetic materials. The magnetization measures the magnetic spins response to magnetic field. The response is produced in a loop called the magnetic hysteresis loop. It is the magnetic spin response to the application and removal of magnetic field. Figure 2.4 shows a schematic diagram of the magnetic hysteresis loop responses from materials with the different main classes of magnetic order in solids.

The M_S can be empirically calculated from the law of approach to saturation magnetization given by [11]:

$$M(H) = M_S\left(1 - \frac{a}{H} - \frac{b}{H^2}\right) + \chi H \quad (1)$$

where a and b are constants, M_S is the saturation magnetization and χ_{hf} is the high field susceptibility. The a/H term is attributed to structural defects or nonmagnetic inclusions. The b/H^2 term is due to uniform magneto-crystalline anisotropy.

The coercivity gives a measure of the anisotropy of a magnetic material [12]. This can be estimated by:

$$H_C = \frac{|H_{C1}| + |H_{C2}|}{2}, \quad (2)$$

where H_{C1} and H_{C2} are the negative and positive coercivity respectively along the magnetic field direction [13]. Soft superparamagnetic materials are expected to have insignificant or almost zero coercivity thereby quenching the propensity for high degree of agglomeration of the nanoparticles and the demand for high magnetic field. This implies that it will be easier to recycle the magnetic nanoparticles after every cycle of magnetization for reuse in the oil spoil cleaning process.

Micro-structural properties such as crystallite size D and lattice parameters a could significantly contribute to changes in structural and magnetic properties of materials [14-15-16]. The Scherrer's formula;

$$D = \frac{K\lambda}{W_{(hkl)}\mathrm{Cos}\theta}, \quad (3)$$

It is often used Equation (3) to estimate D, where K is a constant associated with the shape factor with a value of about 0.94 for a spherical shape, λ is the X-ray diffraction wavelength, W is the full width at half maximum, θ is the Bragg's angle and hkl are the Miller indices of a selected intensity peak [17].

Also, from Bragg's law of diffraction, one could establish that the lattice parameters *a* for a cubic crystal structure has a relationship with hkl as;

$$a = \frac{\lambda}{2\mathrm{Sin}\theta}\sqrt{h^2 + k^2 + l^2}\ . \quad (4)$$

3. MATERIAL AND METHODS

The materials and methodology are presented for the research work.

3.1 Glycol-Thermal Method

The glycol-thermal method is a wet chemical method of synthesizing nanoparticles using a stoichiometric amount of the starting chemical materials in their metal chlorides or nitrates forms. These precursors are usually dissolved in de-ionized water. To precipitate the nitrates or the metal chloride from its solution, sodium hydroxide or ammonia potassium hydroxide is used respectively. The process is kept under continuous stirring condition while the pH value gradually increases until a desired value is reached. After about 40 minutes of continuous stirring, the solution is washed over a thin-pore filter using de-ionized water to remove the chlorides or nitrates. The resulting compound is put inside ethylene glycol and transferred to a pressure reactor for certain duration. A PARR 4843 stirred pressure reactor was used in the current work. The stirring conditions in the reaction chamber such as temperature, speed and pressure are recorded accordingly.

This method was used to synthesize $CoFe_2O_4$ and $ZnFe_2O_4$nano-ferrites in this work. The starting materials are $FeCl_3.6H_2O$ (99%), $CoCl_2.6H_2O$ (98%) and $ZnCl_2.6H_2O$ (98%) as purchased from Sigma-Aldrich. The starting materials are dissolved in about 400 ml of de-ionized water contained in a beaker. The beaker is placed on a magnetic stirrer at different times for the synthesis of $CoFe_2O_4$. Similar process was followed for the synthesis

of $ZnFe_2O_4$nano-ferrites. An initial pH value of 2.51 was recorded and the solution was continuously stirred for about 20 minutes to achieve homogeneity of the mixture. Ammonium solution was carefully used to raise the pH to about 9, causing a precipitation of the metal chlorides. It was maintained under this condition for about 30 minutes. The chloride contained in the precipitate was washed off over a glass microfibre filter in a Büchner funnel using de-ionized water. Standard solution of silver nitrate was used to confirm the absence of chlorides in the filtrate by ensuring that the precipitate of silver chloride was not visible. The recovered precipitate was put in about 250 ml of ethylene glycol and reacted using a pressure reactor. The reaction occurred at a soak temperature of 200 ºC that was retained for 6 hours. The reactor was operated at a speed and pressure of about 300 rpm and 80 psi respectively. Similar process of washing the sample was followed after the reaction was completed. The recovered sample was dried for about 24 hours under an infra-red light to dry up any moisture, collected and stored in a vial.

3.2 Sample Characterization

3.2.1 X-ray Diffraction

X-ray diffraction (XRD) is a technique used to investigate the structural characteristics of crystalline or amorphous materials. It can be applied to identify phases of crystalline structures in a sample. It provides detailed Information about the lattice fringes of crystalline samples often known as *d* spacing. Microstructural information such as crystal orientation, internal stress, crystallite size and shape can be derived from XRD data [18]. The principle of X-ray diffraction is such that when X-rays leave a crystal it causes the incident beam to interfere with each other. However, diffraction only occurs if Bragg's law is satisfied which is mathematically expressed as;

$$n\lambda = 2d\sin\theta, \tag{5}$$

where θ is the angle between the incident beam and the scattering plane, *d* is the interplaner distance, λ is the wavelength of the incident beam and *n* is an integer,. The lattice constant *a* of a cubic crystal has a relationship with the of a sample by the following equation;

$$a = d\sqrt{h^2 + k^2 + l^2}\,. \tag{6}$$

Therefore, substituting Bragg's law into the Equation (6) gives Equation (4). It is from the XRD high intensity peak (311) that the crystallite size of the nanoparticles is estimated using Equation (3).

3.2.2 High Resolution Transmission Electron Microscopy and Scanning Electron Microscopy

The morphology and the physical microstructure of a sample can be studied using high resolution transmission electron microscopy (HRTEM). It is a technique used to study the images of a sample; carry out sample size investigation, shape and crystallographic structures in the micro or nano-nanometer range. The images are generated from electron beams interactions that are transmitted through the sample. The samples are prepared in a thin form for better results. The objective lens magnifies and focuses the images which then appear on an imaging screen which has charge-couple sensor that detects. A Joel-JEM-2100 HRTEM was used to investigate the samples studied in this. A very little sample quantity of about 0.0001 g was dispersed in ethanol and ultrasonically vibrated at 80Hz\40Watt for 3 minutes. A thin film of copper sample holder whose diameter is about 0.0005 mm was put into prepared sample and loaded in the HRTEM equipment for measuements.

Surface morphology of samples is better studied using high resolution scanning electron microscopy (HRSEM). The machine operates with similar principle as that of the HRTEM except that the electron beam is focused on the sample's surface. The strikes of the electron beam on the surface generate signals required for information about the elemental composition of the sample, also referred to as energy dispersive X-ray. A Zeiss ultra plus HRSEM model was used do sample surface scan in this work. The sample preparation performed by depositing very little quantity one side of a sticky carbon tape attached to a sample holder. The sample was coated with gold using a Polaron SC 500 sputter coater to avoid charging by the electron beam.

3.2.3 Magnetization Measurements

A LakeShore vibrating sample magnetometer (VSM) was used to measure the magnetic properties. The sample was measured in a magnetic field of about 14 kOe. The VSM comprise a 735 VSM controller, a vibrating head mounted on a cryostat, a pair of pick-up coils at the faces of the poles of the electromagnet. It also contains a bipolar electromagnet power supply, a Gaussmeter for magnetic field measurements, a temperature controller, a chiller and a data card for data collection.

The VSM operates on the Faraday's law of magnetic induction which is due to the induced voltage that is generated from the pair of pick-up coils. The voltage is proportional to the magnetization of the sample. According to Faraday's law;

$$\frac{d\Theta}{dt} = -E, \tag{7}$$

where $\frac{d\Theta}{dt}$ is the rate of change of magnetic flux and *E* is the induced voltage. This principle helps to measure the magnetic moment by using the AC signal produced from the vibrating magnetized sample. The degree of the magnetization of the sample bears a direct relationship with the amplitude of the induced signal.

3.2.4 ^{57}Fe Mössbauer setup and measurements

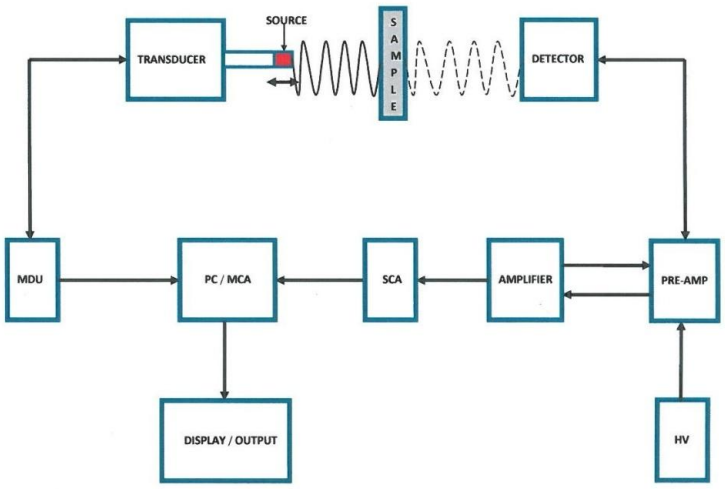

Figure 1. Mössbauer Spectroscopy Block Diagram.

Figure 1 shows a typical block diagram of a 57Fe Mössbauer spectroscopy deployed for the current work. It shows a Mössbauer drive unit (MDU), a CANBERRA amplifier, a pre-amplifier, a power supply, a detector and a multichannel analyzer (MCS). The device contains a 25 mCi ^{57}Co source that is sealed in a Rh matrix and attached to the transducer. The calibration was done at room temperature using an alpha-iron foil. A thin sample of about 0.2 g was sufficient for the measurement. The γ ray of energy intensity of 14.4 keV from the source interacts with the nucleus of the sample and the transmitted rays through the sample are detected by the detector. The signals are therefore amplified at high voltage (HV) and transmitted through a single channel analyser (SCA). They are further processed for data capture using a multi-channel analyzer (MCA). The data are interpreted on the computer screen as Mössbauer spectra. The collection of the data is carried out for a

minimum of about 15 minutes. However, analytical Mössbauer recoil software is used for the data analysis.

4. RESULTS AND DISCUSSION

This section provides details on results and analysis of the magnetic nano ferrites material based on the structural studies, morphological and magnetization measurement.

4.1 X-ray diffraction

The X-ray powder diffraction patterns for $CoFe_2O_4$ and $ZnFe_2O_4$nano-ferrites are shown in Figures 2 and 3 respectively. The XRD instrument used in the current work was equipped with a diffracted beam monochromator in the receiving optics equipped with a Cobalt anode at wavelengths λ_1=1.7892 Å, and λ_2=1.7931 Å. The calculated average wavelength λ was 1.7903 Å. The data were collected in a 2θ-range of 10° to 80° at an angular resolution of 0.02°. The results show that nano-ferrites samples are pure phases without impurities. All the peaks are well indexed with reference to the spinel structure (Joint Committee on Powder Diffraction Standards (JCPDS No. 022-1086) associated with the space group Fd3m [19]. The prominent 311 peak associated with spinel structure can be clearly seen. The broadness of the peaks, especially for the $CoFe_2O_4$ nano-ferrites is indicative of the nano-particle nature of the sample. Therefore, the expectation is that the crystallite size of the $CoFe_2O_4$ nano-ferrites should be smaller compared to that of $ZnFe_2O_4$ nano-ferrites.

The crystal structure analysis were performed using the 311 peak to determine parameters such as the crystallite size *D* and the lattice parameters *a*. The *D* and *a* were calculated using equations 3 and 4 respectively, and the obtained values are presented in Table 3.0. As expected from the broadness of $ZnFe_2O_4$nano-ferrites XRD peaks, the crystallite size of the $ZnFe_2O_4$nano-particles is bigger by about 8 nm compared to $CoFe_2O_4$nano-ferrites. This might not be unconnected to the ionic radii of Co and Zn, which are 125 pm and 137 pm respectively [20]. This implies that Zn with larger ionic radius could lead to expansion of the unit cell of $ZnFe_2O_4$nano-ferrites. The values of the lattice parameters, *a,* are consistent with reported values for ferrite spinel structure. No significant increase was, however, observed for *a* in both samples.

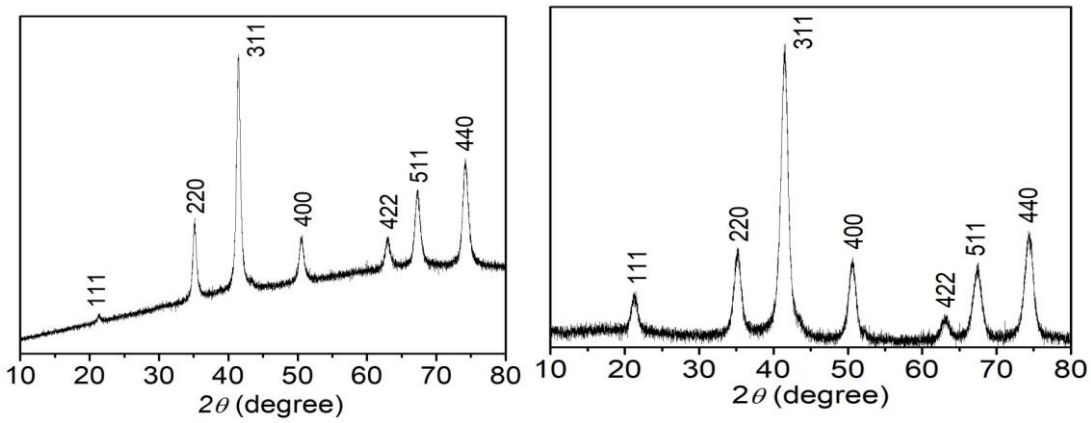

(a) $ZnFe_2O_4$ Ferrites **(b) $CoFe_2O_4$ Ferrites**

Figure 2. X-ray Diffraction patterns for (a) $ZnFe_2O_4$ Ferrites and (b) $CoFe_2O_4$ Ferrites

Table 1. Crystal Structure Parameters, Size (D), lattice parameter (a) for $CoFe_2O_4$ and $ZnFe_2O_4$ Nano-Ferrites

Sample	*D* (nm)±0.24	*a* (Å)±0.005	R^2
$CoFe_2O_4$	10.04	8.384	0.9869
$ZnFe_2O_4$	17.82	8.386	0.9871

4.2 Morphological Studies

The shape of the nano-particles and their surface were examined using high resolution transmission electron microscopy and high resolution scanning electron microscopy (HRTEM and HRSEM) respectively. The morphologies of the samples are shown in Figures 2 and 3.respectively The nano-ferrites sample of $CoFe_2O_4$ shows a better crystalline structure with particles of almost spherical shape compared to $ZnFe_2O_4$nano-ferrites. The HRSEM images of both nano-ferrites measured at the same magnification of 100 nm reveal that the particle sizes of the $ZnFe_2O_4$nano-ferrites are bigger than that of

$CoFe_2O_4$nano-ferrites. This supports the crystallite size estimation from the XRD data. The surface images also show the fairly spherical nature of the nano-particles.

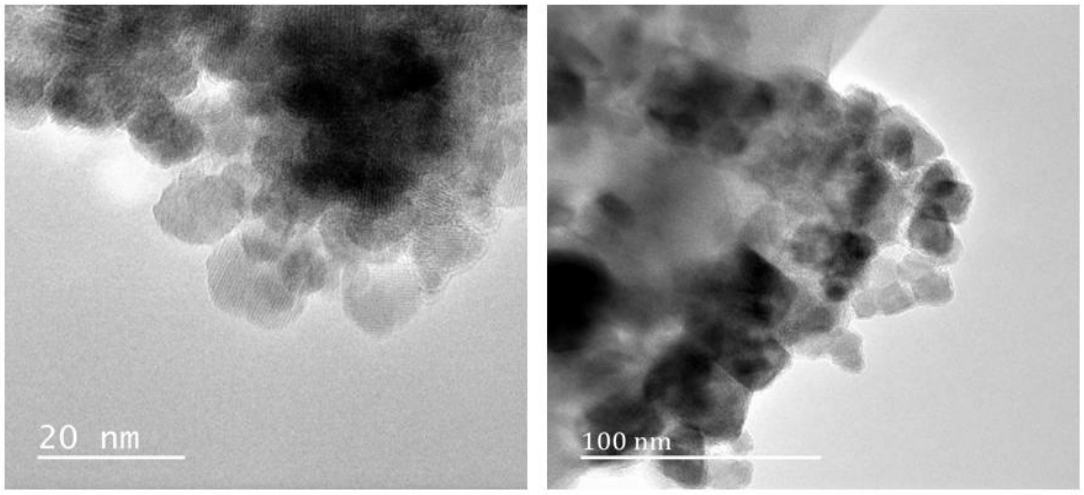

(a) HRTEM image of $CoFe_2O_4$ Nano-Ferrites (b) HRTEM image of $ZnFe_2O_4$ Nano-Ferrites

Figure 3. HRTEM image of Nano-Ferrites Synthesized by Glycol-Thermal Method

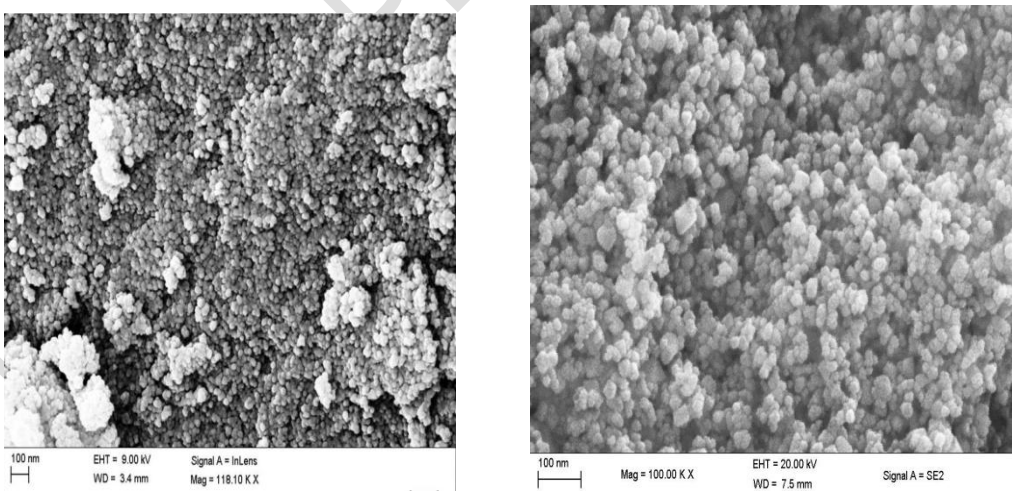

(a) HRSEM image of $CoFe_2O_4$ Nano-Ferrites (b) HRSEM image of $ZnFe_2O_4$ Nano-Ferrites

Figure 4. HRSEM image of Nano-Ferrites Synthesized by Glycol-Thermal Method

4.3 Magnetization Measurements

Magnetization measurements at room temperature were performed on the nano-ferrites samples, using LakeShore model 735 VSM equipment. The magnetic properties such as coercivity H_C and saturation magnetizat sizes as already shown in the VSM results. Similar magnetization results for $CoFe_2O_4$ have been reported by Xing-Hua *et. al.* [22] M_S were estimated from magnetic hysteresis loops. The H_C and M_S were estimated based on Equations 2 and Equation 1 respectively. The magnetic hysteresis loop for $CoFe_2O_4$ nano-ferrites is presented in Figure 4 (a). The fit is shown in Figure 4(b). The hysteresis loop show evidence of superparamagnetic behavior associated with smaller particle. The nano-ferrite had coercivity H_C of about 0.03 kOe and saturation magnetization M_S of about 50 emu/g. These features are desirous for practical application of nano-particles for oil spill cleanup. The implication is that a small magnet will be sufficient to magnetize and demagnetize the sample without significant remnant or residual magnetization in the sample. It also implies that during the recycling process of the nano-particles, magnet with little magnetic field strength can help perform the cycle of magnetization with swift response to the magnetic field.

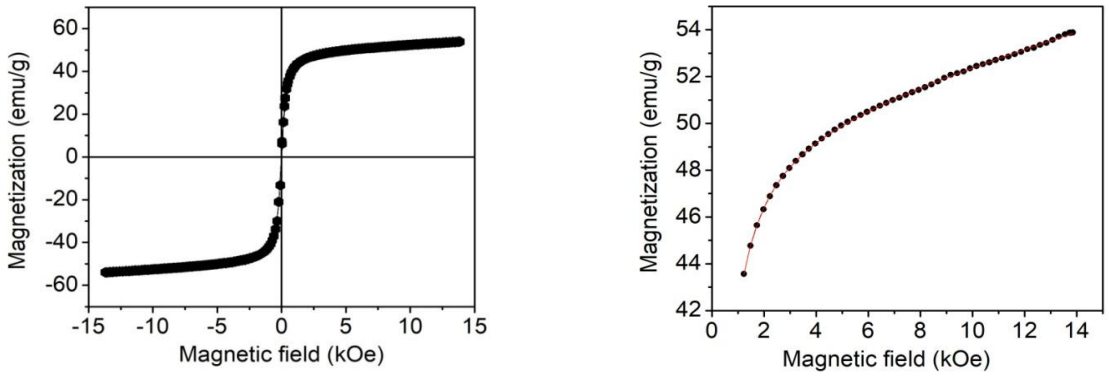

(a) (b)

Figure 5. (a) Room Temperature hysteresis loops of $CoFe_2O_4$nano-ferrites, (b) A fit Approach to Saturation Magnetization of the High Field initial Magnetization of $CoFe_2O_4$ (Equation 1).

Similar analysis was performed on the $ZnFe_2O_4$ nano-ferrites particles. The hysteresis loop is presented in Figure 5(a). The magnetic loop appears to show mixed magnetic phases of super-paramagnetism and paramagnetism. The paramagnetic component can be observed from the steep shape of the hysteresis loop. Coercivity, H_C, of about 0.20 kOe and saturation magnetization M_S of about 30 emu/g were obtained. The low magnetization value when compare to that obtained for $CoFe_2O_4$ nano-ferrites could be attributed to unpaired electrons in the valence shell of Zn atoms, thereby causing a poor magnetic response of the $ZnFe_2O_4$ nano-ferrites. Thus could also explain why there is a slight increase in the coercivity because, non-magnetic atoms within a cluster of magnetic spins could increase coercivity [23]. Although, $CoFe_2O_4$ nano-ferrites showed the most desirous properties for application, $ZnFe_2O_4$ nano-ferrites is less toxic. Therefore, its response to the application and removal of magnetic field could be slow, it will be environmentally friendly.

The obtained parameters from the fit to the law of approach to saturation magnetization of Equation 1 are presented in Figure 5(b). The significant change in the a parameter for $ZnFe_2O_4$nano-ferrites is indicative of a nonmagnetic inclusions arising from Zn atoms.

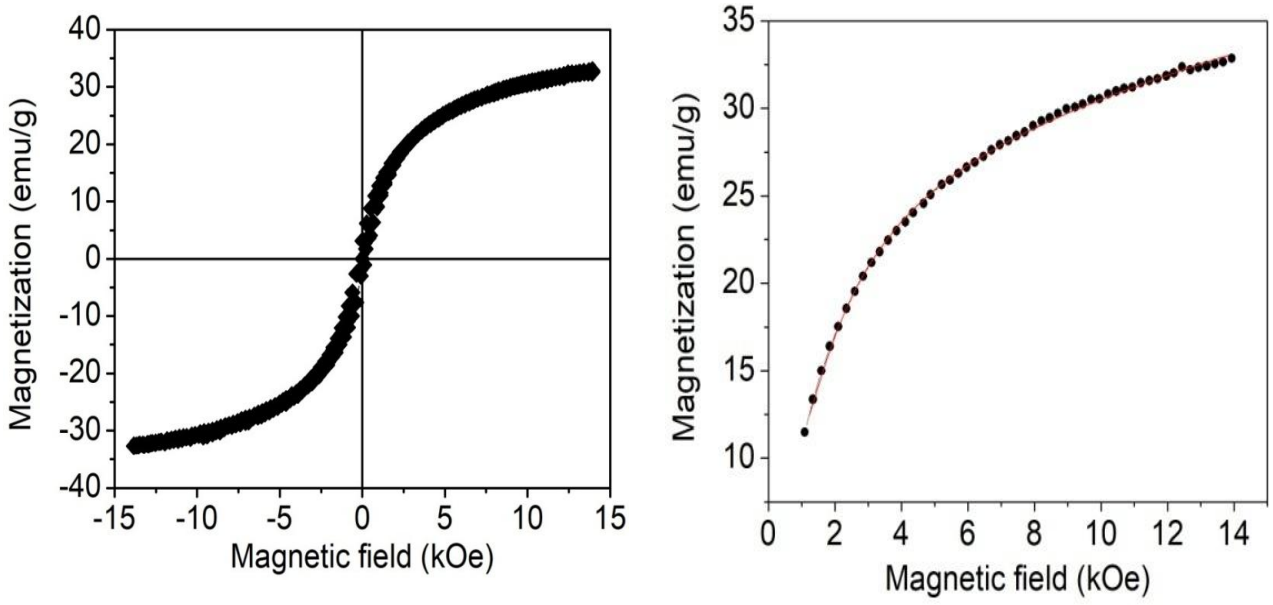

Figure 6. (a) Room Temperature hysteresis loops of $ZnFe_2O_4$nano-ferrites, (b) A fit Approach to Saturation Magnetization of the High Field initial Magnetization of $ZnFe_2O_4$ (Equation 1).

4.4 ^{57}Fe Mössbauer Spectroscopy Measurements

The ^{57}Fe Mössbauer spectroscopy measurements for the $CoFe_2O_4$ and $ZnFe_2O_4$ nano-ferrites were performed at room temperature. α-Fe foil was used for the calibration at a constant acceleration. The Recoil Mössbauer analysis software was used for the fitting of the magnetic components using the Lorentzian site analysis.

Two sextets' δ_1 and δ_2, were best suited to model the $CoFe_2O_4$ nano-ferrites as shown in Figure 6. The spectra shows a well ordered magnetic phase where sextets' δ_1 and δ_2 are associated with Fe^{3+} ions at tetrahedral A-sites and octahedral B-sites of the spinel crystal structure [24]. Table 2 gives the values of the magnetic hyperfine field, H_{Bf}, isomer shift, *IS*, quadrupole splitting, Δ_{EQ}, and the fraction population, *f*, of Fe^{3+} ions. The higher field of about 482 kOe is attributed to the B-sites and the lower field of about 445 kOe associated with the A-sites. The isomer shift values are in the appropriate range for Fe^{3+} [25] and the

hyperfine magnetic field are close to reported values [26]. Therefore, no evidence of Fe^{2+} is observed.

Table 2. Mössbauer parameters of $CoFe_2O_4$nano-ferrites samples obtained from fit, where δ isomer shifts, (*IS*) H_{bf} is the hyperfine magnetic field, quadrupole splitting (Δ_{EQ}), fraction populations (*f*) and reduced chi^2 (R^2) of Fe ions

Sample	Sites	H_{Bf}(kOe)	δ (mm/s)	Δ_{EQ} (mm/s)	*f* (%)	R^2
		±1.3	±0.02	±0.00	±2	1.3110
$CoFe_2O_4$	δ1 (A-site)	445.3	0.31	0.01	30	
	δ2 (B-site)	482.3	0.31	0.01	70	

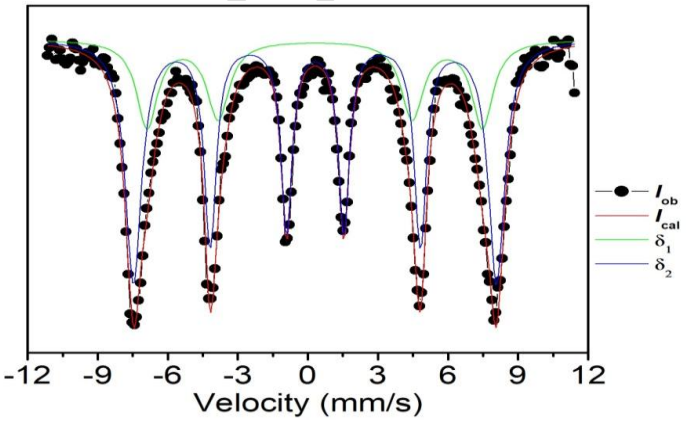

Figure 7. Fit to ^{57}Fe Mössbauer Spectra for $CoFe_2O_4$ Nano-Ferrites.

However, the $ZnFe_2O_4$ nano-ferrite was not a well ordered sextet compared to $CoFe_2O_4$ nano-ferrite, and it was best fitted with two sextets and two doublets as shown in Figure 7. The results are shown in Table 3. The effect of the paramagnetic component can be seen to have a dropping effect and broadness of the spectra. The two sextets are associated with the coordination of Fe^{3+}ions at tetrahedral A and octahedral B sites of the

spinel crystal structure [27]. The doublets account for the paramagnetic component as was observed in the magnetic hysteresis loops. Again, the isomer shift values are in the appropriate range for Fe^{3+}. Higher values of quadrupole splitting indicate that the ions are imbedded in non-cubic surroundings, while the relatively small values of the quadrupole splitting indicate that A and B sites have nearly cubic symmetry.

Table 3. Mössbauer parameters obtained from fit, where H_{bf} is the hyperfine magnetic field, δ isomer shifts (*IS*), quadrupole splitting (Δ_{EQ}), fraction populations (*f*) and reduced chi^2 (R^2) of Fe ions of $ZnFe_2O_4$nano-ferrites samples.

Sample	Sites	H_{Bf}(kOe)	δ (mm/s)	Δ_{EQ} (mm/s)	*f* (%)	R^2
		±1.2	±0.02	±0.00	±1	
$ZnFe_2O_4$	δ1 (A-site)	408	0.32	0.00	24	1.1102
	δ2 (B-site)	470	0.31	-0.00	15	
	D_1		0.37	7.22	30	
	D_2		0.35	1.03	32	

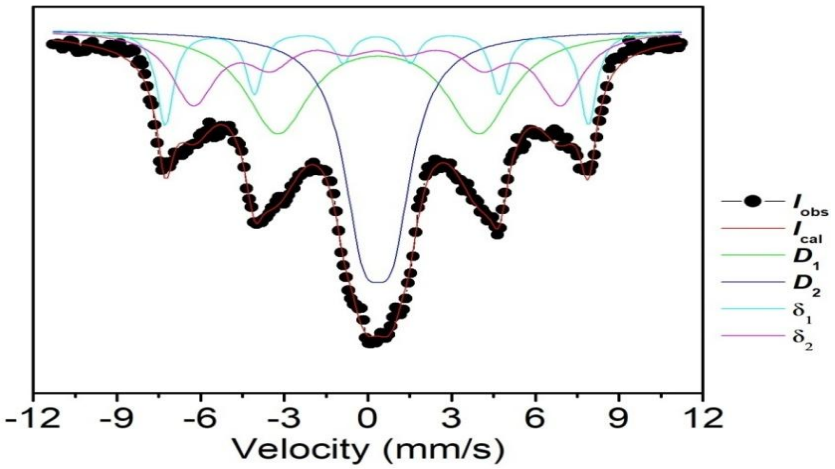

Figure 8. Fit to ^{57}Fe Mössbauer spectra for $ZnFe_2O_4$nano-ferrites

5. CONCLUSIONS

Magnetic nano-particles possess the potential to be used for environmental remediation. Certain magnetic properties are expected for such application. This work studied the structural and magnetic properties of $CoFe_2O_4$ and $ZnFe_2O_4$nano-ferrites synthesized by glycol-thermal technique. The properties that support their application for oil spill cleanup are considered. Structural properties were investigated by X-ray diffraction technique from which information such as crystallite size and lattice parameters were determined. The $CoFe_2O_4$ and $ZnFe_2O_4$nano-ferrites samples were single phase cubic spinel structure without any impurity phase. Larger crystallite size of about 17 nm was obtained for $ZnFe_2O_4$nano-ferrites compared to about 10 nm obtained for $CoFe_2O_4$nano-ferrites. Such large size was attributed to lager atomic radii of Zn atoms. No significant changes occurred in the lattice parameters. The high resolution transmission electron microscopy and surface microscopy showed that nano structure and the almost-spherical shape of the nanoparticles.

Room temperature magnetization results of the two samples show evidence of superparamagnetic behavior for $CoFe_2O_4$nano-ferrites. However, a mixed magnetic phase of superparamagnetism and paramagnetism appear to be the case for $ZnFe_2O_4$ nano-ferrites. $CoFe_2O_4$ has a low coercivity and high magnetization compared to $ZnFe_2O_4$ nano-ferrites. This suggests that the nanoparticles will respond to small magnetic field when such particles are used for environmental remediation such as oil spill cleanup. However, it has a disadvantage of toxicity at high concentration dosage compared to $ZnFe_2O_4$ nano-ferrites that is environmentally friendly. Hence, $ZnFe_2O_4$ nano-ferrites might have a slow response to magnetic field, it possess higher potential for environmental sustainable when considering the two samples studied in this work. The room temperature ^{57}Fe Mössbauer spectra show ordered magnetic structures for $CoFe_2O_4$ that were resolved with two sextets. The internal magnetic field splitting and isomer shifts values are consistent with that of ferrites. The evidence of paramagnetic component in $ZnFe_2O_4$ nano-ferrites was further revealed by the ^{57}Fe Mössbauer measurements. Two sextets and two doublets were used to resolve the

spectra. Isomer shifts on A-, B- and doublet sites are consistent with Fe^{3+} ions. No evidence of other oxidation state of Fe was seen. The hyperfine fields based on the Lorentzian site analysis for $ZnFe_2O_4$ nano-ferrites were lower compared to $CoFe_2O_4$ nano-ferrites. The glycol-thermal synthesis method is a viable method to produce nano-ferrites with single phase.

From the single phase of $CoFe_2O_4$ nano-ferrites and $ZnFe_2O_4$ nano-ferrites which ware synthesized by glycol-thermal method at 200 ºC we are able to show from ^{57}Fe Mössbauer spectroscopy measurement that the oxidation state of Fe was stable at Fe^{3+} such stability in the oxidation state of Fe helps in reusability of the nanoparticles after every cycle of clean up. This is important because the magnetic properties of the nanoparticles can be fairly predicted not change significantly to affect its application around room temperature. We are also able to find that $CoFe_2O_4$has a low desirable coercivity property making it a better candidate for possible oil spill cleanup compared to the $ZnFe_2O_4$studied in the current work.

COMPETING INTERESTS DISCLAIMER:

Authors have declared that no competing interests exist. The products used for this research are commonly and predominantly use products in our area of research and country. There is absolutely no conflict of interest between the authors and producers of the products because we do not intend to use these products as an avenue for any litigation but for the advancement of knowledge. Also, the research was not funded by the producing company rather it was funded by personal efforts of the authors.

REFERENCES

1. Kirubakaran S, Thiruvenkatam V. Diverse applications of nanotechnology in biomedicine, chemistry, and engineering. InHandbook of Research on Diverse Applications of Nanotechnology in Biomedicine, Chemistry, and Engineering 2015 (pp. 1-9). IGI Global.

2. Khalil, Munawar, Badrul Mohamed Jan, Chong Wen Tong, and Mohammed Ali Berawi. "Advanced nanomaterials in oil and gas industry: design, application and challenges." Applied energy 191 (2017): 287-310.

3. Ko S, Kim ES, Park S, Daigle H, Milner TE, Huh C, Bennetzen MV, Geremia GA. Amine functionalized magnetic nanoparticles for removal of oil droplets from produced water and accelerated magnetic separation. Journal of Nanoparticle Research. 2017 Apr 1; 19(4):132.

4. Fakoya MF, Shah SN. Emergence of nanotechnology in the oil and gas industry: Emphasis on the application of silica nanoparticles. Petroleum. 2017 Dec 1;3(4):391-405.

5. El-Diasty A, Ibrahim, and Adel M. Salem Ra.lo00gab. "Applications of nanotechnology in the oil & gas industry: Latest trends worldwide & future challenges in Egypt." In *North Africa Technical Conference and Exhibition*. Society of Petroleum Engineers, 2013.

6. Valenzuela FJ, Pérez-Sepúlveda A, Torres MJ, Correa P, Repetto GM, Illanes SE. Pathogenesis of preeclampsia: the genetic component. Journal of pregnancy. 2012 Sep 18; 2012.

7. Pandey B, Litterst FJ, Baggio-Saitovitch EM. Preferential spin canting in nanosize zinc ferrite. Journal of Magnetism and Magnetic Materials. 2015 Jul 1; 385:412-7.

8. Hill PM, Peiser HS, Rait JR. The crystal structure of calcium ferrite and β calcium chromite. Acta Crystallographica. 1956 Dec 10;9(12):981-6.

9. Ramarao K, Rajesh Babu B, Kishore Babu B, Veeraiah V, Ramarao SD, Rajasekhar K, Venkateswara Rao A. Influence of Zn Substitution on Structural,

Magnetic and Electrical Properties of MgFe 2 O 4. Journal of Electronic Materials. 2018 May 1;47(5)..

10. Msomi JZ, Dlamini WB, Moyo T, Ezekiel P. Investigation of phase formation of (Zn, Mg) 0.5 Co0. 5Fe2O4 nanoferrites. Journal of Magnetism and Magnetic Materials. 2015 Jan 1; 373:68-73.

11. Andreev SV, Bartashevich MI, Pushkarsky VI, Maltsev VN, Pamyatnykh LA, Tarasov EN, Kudrevatykh NV, Goto T. Law of approach to saturation in highly anisotropic ferromagnets Application to Nd□ Fe□ B melt-spun ribbons. Journal of alloys and compounds. 1997 Sep 12;260(1-2):196-200.

12. Guo X, Chen X, Altounian Z, Ström-Olsen JO. Temperature dependence of coercivity in MnBi. Journal of applied physics. 1993 May 15; 73(10):6275-7..

13. Simonsen G, Strand M, Øye G. Potential applications of magnetic nanoparticles within separation in the petroleum industry. Journal of Petroleum Science and Engineering. 2018 Jun 1;165:488-95

14. Kodama RH. Magnetic nanoparticles. Journal of magnetism and magnetic materials. 1999 Oct 1;200(1-3):359-72..

15. Rocco DL, Coelho AA, Gama S, Santos MD. Dependence of the magnetocaloric effect on the A-site ionic radius in isoelectronic manganites. Journal of Applied Physics. 2013 Mar 21; 113(11):113907.

16. Rostamnejadi A, Venkatesan M, Kameli P, Salamati H, Coey JM. Magnetocaloric effect in La0. 67Sr0. 33MnO3 manganite above room temperature. Journal of Magnetism and Magnetic Materials. 2011 Aug 1; 323(16):2214-8.

17. Kittel C, McEuen P, McEuen P. Introduction to solid state physics. New York: Wiley; 1996 Dec.

18. Cullity BD. Elements of X-ray Diffraction. Addison-Wesley Publishing; 1956.

19. Park CH, Na JG, Heo NH, Lee SR, Kim J, Park K. Characterization of Metal/Cobalt Ferrite Magnetic Thin Films. Journal of Magnetics. 1998;3(1):31-5.

20. Wells AF. Structural inorganic chemistry. Oxford university press; 2012 Jul 12.

21. Li XH, Xu CL, Han XH, Qiao L, Wang T, Li FS. Synthesis and magnetic properties of nearly monodisperse CoFe 2 O 4 nanoparticles through a simple hydrothermal condition. Nanoscale research letters. 2010 Jun; 5(6):1039-44..

22. Li Q, Kartikowati CW, Horie S, Ogi T, Iwaki T, Okuyama K. Correlation between particle size/domain structure and magnetic properties of highly crystalline Fe 3 O 4 nanoparticles. Scientific reports. 2017 Aug 30; 7(1):1-7.

23. Coey JM. Hard magnetic materials: A perspective. IEEE Transactions on magnetics. 2011 Sep 1; 47(12):4671-81.

24. Gismelseed AM, Mohammed KA, Widatallah HM, Al-Rawas AD, Elzain ME, Yousif AA. Structure and magnetic properties of the ZnxMg1-xFe2O4 ferrites. InJournal of Physics: Conference Series 2010 Mar 1 (Vol. 217, No. 1, p. 012138). IOP Publishing.

25. Rao BP, Rao PS, Murthy GV, Rao KH. Mössbauer study of the system Ni0. 65Zn0. 35Fe2− xScxO4. Journal of magnetism and magnetic materials. 2004 Jan 1; 268(3):315-20.

26. Johnson CE, Ridout MS, Cranshaw TE. The Mössbauer effect in iron alloys. Proceedings of the Physical Society (1958-1967). 1963 Jun 1; 81(6):1079.

27. Pankhurst QA, Pollard RJ. Origin of the spin-canting anomaly in small ferrimagnetic particles. Physical review letters. 1991 Jul 8; 67(2):248.